The Mass-Discrepancy Acceleration Relation: a Natural Outcome of Galaxy Formation in CDM halos

Aaron D. Ludlow,* Alejandro Benítez-Llambay, Matthieu Schaller, Tom Theuns, Carlos S. Frenk, and Richard Bower
Institute for Computational Cosmology, Department of Physics, Durham University, Durham DH1 3LE, U.K.

Joop Schaye
Leiden Observatory, Leiden University, PO Box 9513, 2300 RA Leiden, the Netherlands

Robert A. Crain
Astrophysics Research Institute, Liverpool John Moores University, 146 Brownlow Hill, Liverpool, L3 5RF

Julio F. Navarro,† Azadeh Fattahi, and Kyle A. Oman
Department of Physics and Astronomy, University of Victoria, PO Box 1700 STN CSC, Victoria, BC, V8W 2Y2, Canada
(Dated: December 23, 2017)

We analyze the total and baryonic acceleration profiles of a set of well-resolved galaxies identified in the EAGLE suite of hydrodynamic simulations. Our runs start from the same initial conditions but adopt different subgrid models for stellar and AGN feedback, resulting in diverse populations of galaxies by the present day. Some of them reproduce observed galaxy scaling relations, while others do not. However, regardless of the feedback implementation, all of our galaxies follow closely a simple relationship between the total and baryonic acceleration profiles, consistent with recent observations of rotationally supported galaxies. The relation has small scatter: different feedback processes – which produce different galaxy populations – mainly shift galaxies along the relation, rather than perpendicular to it. Furthermore, galaxies exhibit a single characteristic acceleration, $g_\dagger$, above which baryons dominate the mass budget, as observed. These observations have been hailed as evidence for modified Newtonian dynamics but can be accommodated within the standard cold dark matter paradigm.

INTRODUCTION

In the standard cosmological paradigm, the matter content of the Universe is dominated by cold dark matter (CDM). In this CDM model structures form hierarchically through repeated merging and continuous smooth accretion [e.g., 1]. The resultant dark matter (DM) "halos" are the sites of galaxy formation: their deep potential wells can trap gas, which cools and forms stars, providing visible tracers of the underlying DM density field [2, 3].

Understanding the connection between galaxies and their DM halos is of fundamental importance to studies of both the large- and small-scale structure of the Universe. Traditionally this link has been expressed in terms of scaling relations between the structural properties of galaxies and their halos; the Tully-Fisher [4, TF] and Faber-Jackson [5] relations, in particular, relate the luminosity (or stellar mass) of a galaxy to its dynamics which, in the CDM paradigm, is largely governed by its dominant DM halo. Both empirical relations highlight a close connection between galaxies and their halos.

Galaxy formation models based on CDM do not reproduce these relations unless sub-grid models for unresolved feedback are calibrated to form realistic galaxies when judged according to other diagnostics [e.g., 6, 7]. It comes as a surprise, then, that observations reveal an even closer coupling between the luminous mass of galaxies and their total *dynamical* mass. Perhaps most unexpected is the "mass discrepancy-acceleration relation" (MDAR) [8, 9], a tight empirical relation between the radial dependence of the enclosed baryonic-to-dynamical mass ratio and the baryonic centripetal acceleration for rotationally supported galaxies. It has an intrinsic scatter consistent with observational errors alone and holds for galaxies of widely varying luminosity and gas fraction. The MDAR may be expressed empirically as [10]

$$\frac{g_{\rm tot}(r)}{g_{\rm bar}(r)} = \frac{{\rm M}_{\rm tot}(r)}{{\rm M}_{\rm bar}(r)} = \frac{1}{1-e^{-\sqrt{g_{\rm bar}/g_\dagger}}}, \qquad (1)$$

where $g_i(r)$ and ${\rm M}_i(r)$ are, respectively, the centripetal acceleration and enclosed mass profiles.

It has been claimed [see 11, and discussion therein] that the small scatter in the MDAR is inconsistent with hierarchical galaxy formation models, which predict that galaxies should exhibit a broad range of properties even for halos of fixed mass. Furthermore, the MDAR implies a *characteristic* acceleration ($g_\dagger \approx 10^{-10}\,{\rm m\,s^{-2}}$) above which each galaxy's dynamics can be determined by the observed light alone.

Why would baryons and dark matter "conspire" to produce such a characteristic physical scale? One possibility is that galaxies adhere to *modified Newtonian dynamics* (MOND), which naturally gives rise to the MDAR. If true, this result would demand an unconditional rewrite of our established theory of gravity, and would percolate through virtually all aspects of cosmology, astrophysics and fundamental physics.

This possibility should be taken seriously. However, theoretical studies suggest that the MDAR arises naturally in CDM models of galaxy formation, provided they also match observed galaxy scaling relations [12–14] (possibly with larger than observed scatter [15]). In this letter we address these is-

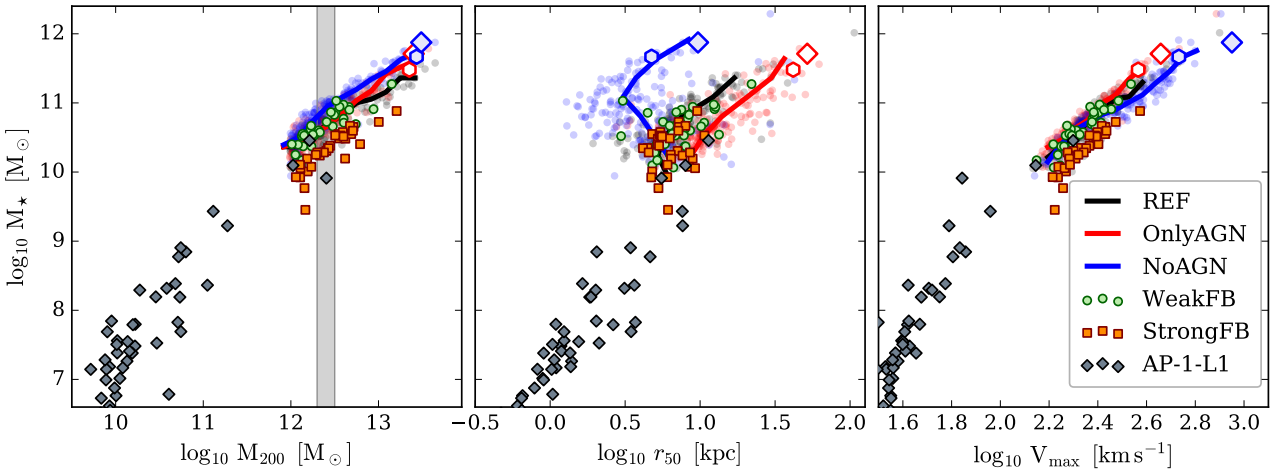

FIG. 1. Relationship between galaxy stellar mass and, respectively, halo virial mass (left), stellar half-mass radius (middle) and maximum circular velocity, $\mathrm{V_{max}}$ (right) for EAGLE and APOSTLE galaxies whose halos are resolved with $\mathrm{N_{200}} \geq 10^5$ DM particles. Solid black lines show the median trends for the "Reference" model (REF); blue and red lines show, respectively, the variations if feedback is entirely limited to AGN (OnlyAGN) or to stars (NoAGN). Semi-transparent dots of the same color show individual halos. Individual halos are also shown for runs with strong (StrongFB, orange squares) and weak (WeakFB, green circles) stellar feedback, and for APOSTLE galaxies (grey diamonds). The heavy open blue and red symbols identify two halos that have been cross-matched and whose circular velocity and acceleration profiles are shown in Figure 2. Figure 2 also shows the average $\mathrm{V_c}(r)$ and $g(r)$ profiles for galaxies in NoAGN and StongFB that fall in the vertical shaded band in the left-most panel.

sues using a suite of hydrodynamical simulations drawn from the EAGLE Project [16]. Our simulations vary the subgrid feedback in a way that strongly modifies the end product of galaxy formation, enabling us to robustly to assess the MDAR for a range of hierarchical galaxy formation "models".

SIMULATIONS AND ANALYSIS

The EAGLE Simulations

Our analysis focuses on well-resolved halos and their central galaxies in the EAGLE simulations [16, 17], all of which model galaxy assembly within the CDM framework. Cosmological parameters are those inferred by the Planck Collaboration [18]: $\Omega_\mathrm{M} = 0.307$, $\Omega_\Lambda = 0.693$, $\Omega_{bar} = 0.04825$, $\mathrm{H_0} = 67.77\,\mathrm{km\,s^{-1}/Mpc^{-1}}$ and $\sigma_8 = 0.8288$. Here Ω_i denotes the fractional contribution to the critical energy density ($\rho_\mathrm{crit} = 3{\mathrm{H_0}}^2/8\pi\mathrm{G}$) from constituent i; $\mathrm{H_0}$ is the present-day Hubble parameter, and σ_8 the rms linear theory mass fluctuation in 8 Mpc/h spheres.

For the purposes of this letter we focus on a subset of the "intermediate resolution" EAGLE simulations (following the nomenclature in [16]). These include periodic volumes of side-length $L_\mathrm{cube} = 25$ and 50 comoving Mpc sampled with, respectively, $\mathrm{N} = 376^3$ and 752^3 particles of both gas and DM. The respective particle masses are $m_\mathrm{g} = 1.81 \times 10^6 \mathrm{M_\odot}$ and $m_\mathrm{dm} = 9.70 \times 10^6 \mathrm{M_\odot}$; the (Plummer-equivalent) softening length is $\epsilon = 0.7$ physical kpc below $z = 2.8$, and 2.66 comoving kpc at higher redshift. Runs for each given cube size always start from the same linear density field and have a corresponding run that includes only DM (with $\Omega^{'}_\mathrm{M} = \Omega_\mathrm{M} + \Omega_\mathrm{bar}$ and $\Omega^{'}_\mathrm{bar} = 0$).

The simulations were performed with a version of the N-body TreePM smoothed particle hydrodynamics code GADGET3 [19] incorporating significantly modified hydrodynamic scheme, time-stepping criteria and subgrid physics modules for radiative cooling, star formation, stellar mass loss, energetic stellar feedback and black hole growth [see 16, for details]. For a given boxsize, our simulations all start from the same initial conditions but adopt different values of the subgrid parameters. As a result, some accurately reproduce a diverse set of low- and high-redshift observations of the galaxy population (such as the global stellar mass function and its dependence on z; galaxy shapes, sizes, and their relationship to stellar mass), whereas others do not.

As discussed in detail by [16], some calibration of the model parameters must be carried out so that simulations (if desired) reproduce a diagnostic set of observational data. For the EAGLE programme, this was achieved by calibrating the feedback models (including contributions from both active galactic nuclei, AGN, and stars) so that the observed galaxy stellar mass function and the mass-size relation were recovered. One such model is the "reference" model (hereafter REF; [16]). Variations of this model systematically changing the subgrid parameters were also carried out [17]. These include runs with weak (WeakFB) or strong (StrongFB) feedback from stars, as well as runs with no AGN feedback (NoAGN), and another with *only* AGN feedback but none from stars (OnlyAGN). The statistics of the resulting galaxy populations depend sensitively on these feedback choices.

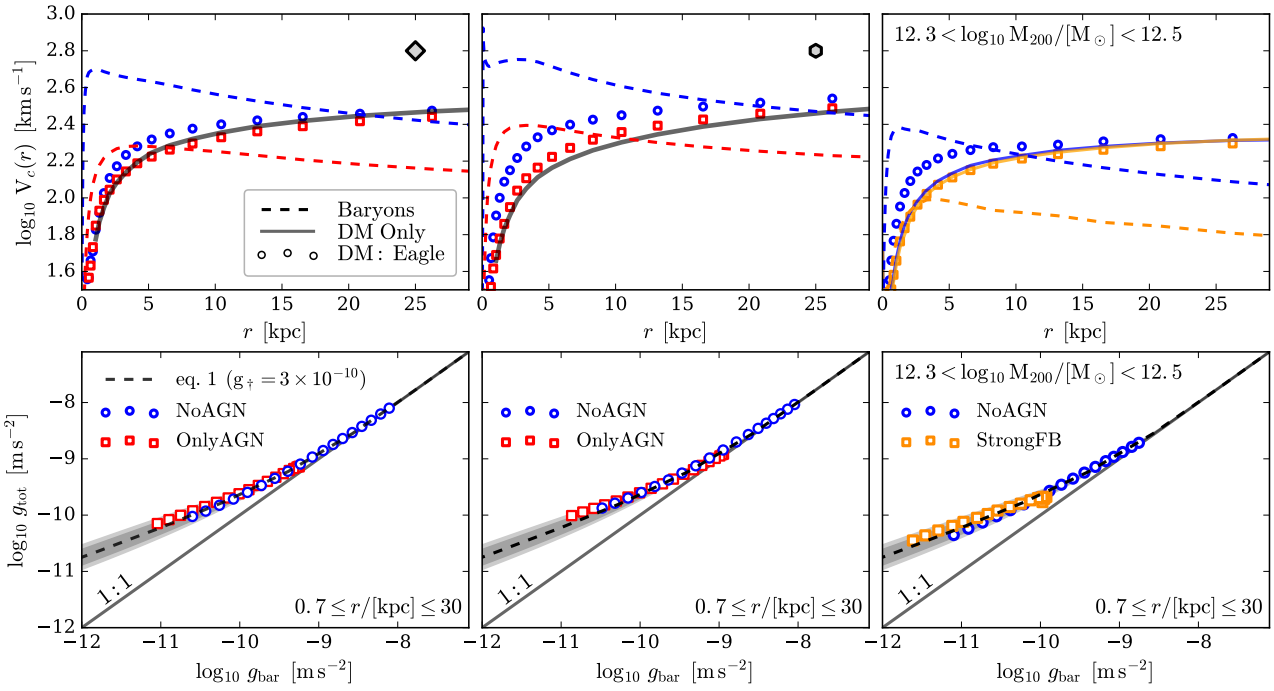

FIG. 2. (Upper panels) Circular velocity profiles for the two galaxies and halos highlighted in Figure 1. Red colors (left and middle panels) indicate the NoAGN and blue the OnlyAGN model. The circular velocity profiles of each galaxy's baryonic component are shown as dashed lines, with points indicating that of the DM halo. (For comparison, the solid black lines show the circular velocity profiles for the same halo identified in the corresponding DM-only simulation.) The lower panels show the acceleration ($g_{\rm bar}$ versus $g_{\rm tot}$) diagrams for these halos. Again, blue (circles) and red (squares) distinguish the NoAGN and OnlyAGN models. Note that only radii spanning $\epsilon \leq r \leq 30\,[\mathrm{kpc}]$ have been plotted (as in the upper panels). For comparison, the linear scaling is shown as a solid black line and eq. 1 as a dashed line (using $g_\dagger = 3 \times 10^{-10}\,\mathrm{m\,s^{-2}}$); shaded regions indicate the scatter around this line brought about by changing the enclosed baryon mass by factors of ± 3 (light) and ± 2 (dark). Panels on the far right show the equivalent *median* profiles for all halos in our NoAGN and StrongFB models that fall in the narrow mass range $12.3 \leq \log_{10}\,\mathrm{M_{200}}/[\mathrm{M_\odot}] \leq 12.5$ (shown as a vertical shaded band in Figure 1).

Analysis

Halo Finding and Selection

All simulations were post-processed with the halo finding algorithm SUBFIND [20, 21], which is used to identify both DM halos and their *central* galaxies (see [16] for details; note that we do not consider "satellite" galaxies in our analysis). For each halo we retain the position of the particle with the minimum potential energy and identify it with the halo and galaxy center. We also record the virial mass $\mathrm{M_{200}}$, and maximum circular velocity, $\mathrm{V_{max}}$. (We define $\mathrm{M_{200}}$ as the mass enclosed by a sphere surrounding each halo center whose density contrast is $200 \times \rho_{\rm crit}$. This implicitly defines the virial radius through $\mathrm{M_{200}} = (800/3)\pi\, r_{200}^3\, \rho_{\rm crit}(z)$.) Both $\mathrm{M_{200}}$ and $\mathrm{V_{max}}$ are calculated using the full matter distribution.

To preclude resolution concerns, we focus our analysis on well-resolved central galaxies whose DM halos are resolved with at least $\mathrm{N_{200}} \geq 10^5$ particles ($\mathrm{N_{200}}$ is the number of DM particles within r_{200}). We impose no isolation or relaxation criteria. Our REF, NoAGN and OnlyAGN runs have, respectively, 187, 192 and 175 halos above this mass threshold; the StrongFB and WeakFB models have 32 and 34, respectively.

To extend the dynamic range of our analysis, we also include *isolated* galaxies identified in the AP-1-L1 simulation [22, see] from the APOSTLE suite (see [23] for details of the APOSTLE Project), which used the same model as EAGLE and the REF subgrid parameters. These 29 galaxies span the (stellar) mass range $1.3 \times 10^7 \lesssim \mathrm{M/M_\odot} \lesssim 2.6 \times 10^9$, have $\mathrm{N_{200}} > 10^5$ and are separated from any other halo whose virial mass exceeds $5 \times 10^{11}\mathrm{M_\odot}$ by at least two virial radii of the more massive system.

Radial Mass profiles of Baryons and Dark Matter

The centripetal acceleration profile due to component i is computed as

$$g_i(r) = \frac{\mathrm{V}_c^i(r)^2}{r} = \frac{\mathrm{G\,M}_i(r)}{r^2}, \qquad (2)$$

where $\mathrm{V}_c^i(r)$ and $\mathrm{M}_i(r)$ are the corresponding circular velocity and enclosed mass profiles, and G is Newton's gravitational constant. When computing $\mathrm{M}_i(r)$ we use *all* particles of component i and not just those deemed by SUBFIND to be bound to the central galaxy. We choose logarithmically-

spaced bins with fixed separations, $\Delta \log_{10} r = 0.1$, spanning $r_{\rm min} = \epsilon$ to $r_{\rm max} \approx 30\,{\rm kpc}$. We have verified that our results are robust to reasonable changes in $r_{\rm max}$. Setting $r_{\rm max} = 0.1 - 0.2 \times r_{200}$, for example, gives results quantitatively consistent with those presented here.

For each galaxy we also record a few diagnostic quantities. Its stellar mass, $\rm M_\star$, is defined as the total mass of stars *bound* to the central galaxy; the stellar half-mass radius, r_{50}, is defined by $\rm M(r_{50})/M_\star = 1/2$.

RESULTS

Figure 1 summarizes several scaling relations for our EAGLE and APOSTLE galaxy samples. The leftmost panel plots galaxy stellar mass versus halo virial mass. Solid lines show the median trends for the 50 Mpc cubes (REF, NoAGN and OnlyAGN models). Individual galaxies are shown as faint circles of corresponding color. Additional runs with strong and weak stellar feedback are also shown, along with the APOSTLE galaxies (in these cases, only individual halos are plotted). The middle and right-hand panels show, using the same color scheme, the stellar mass versus half (stellar) mass radius (middle) and versus peak circular velocity, $\rm V_{max}$ (right).

Different subgrid models clearly produce different galaxy populations. For a given halo mass the median galaxy *stellar mass* spans a factor of ≈ 4 between the two most extreme runs (compare NoAGN and StrongFB in the left-most panel of this Figure). Galaxy sizes also differ, particularly for runs without (NoAGN) and with *only* (OnlyAGN) AGN feedback. Galaxies with stellar masses above $\sim 10^{11}\rm M_\odot$, for example, have half-mass radii that are roughly an order of magnitude smaller when AGN feedback is ignored. The $\rm M_\star$-versus-$\rm V_{max}$ relations of our simulations have, at these mass scales, a zero-point that varies by a factor of ≈ 3.

Figure 2 (upper panels) provides a few examples of the circular velocity profiles of baryons (dashed curves) and dark matter (open symbols) for several galaxies in our sample. The left and middle panels show two massive galaxies that were cross-matched in the NoAGN and OnlyAGN runs (highlighted as outsized points in Figure 1). Because they inhabit the same DM halo their merger histories are similar, but their stellar masses, half-mass radii and peak circular velocities differ noticeably as a result of the differing feedback processes. Each galaxy's DM distribution reflects its response to galaxy formation: the more massive the central galaxy, the more concentrated its DM halo. The effect is, however, weak. The solid black line in each panel shows, for comparison, the circular velocity curve of the same halo in the corresponding DM-only simulation.

Despite these structural differences, all four galaxies follow closely the same relation between the total acceleration and the acceleration due to baryons (bottom left and middle panels). Galaxies in the NoAGN run (blue points and curves), whose central galaxies are both more massive and more compact than those in OnlyAGN, populate the high acceleration regime of the relation, indicating that these galaxies are baryon dominated over a larger radial extent. When included, AGN feedback periodically quenches star formation resulting in less compact and lower mass central galaxies that are DM dominated over a large radial range.

The right-hand panels of Figure 2 show another example. Here we select all halos from the NoAGN and StrongFB runs whose virial masses lie in the range $12.3 \leq \log_{10} \rm M_{200}/M_\odot \leq 12.5$ (shown as a vertical shaded band in the left panel of Figure 1) and plot their *median* circular velocity and acceleration profiles. These galaxies have total stellar masses that differ, on average, by a factor of ≈ 4 depending on the feedback implementation, but inhabit halos of comparable DM mass. As before, solid curves show the median dark matter mass profile for the same halos identified in the corresponding DM-only simulation; open symbols show $\rm V_c^{DM}(r)$ measured directly in the EAGLE runs. The suppression of star formation by strong feedback results in considerably less massive galaxies whose mass profiles are dark matter dominated at most resolved radii. Nevertheless, both sets of galaxies follow the acceleration relation given by eq. 1. (We note that our EAGLE galaxies prefer $g_\dagger \approx 3 \times 10^{-10}\,\rm m\,s^{-2}$, a factor of 2.5 larger than that obtained by [10] from observations of rotationally supported galaxies. This systematic may be related to the details of observational sample selection, the assumed mass-to-light ratio, or differences in how acceleration profiles are inferred from the observed and simulated data.)

In all cases, *different feedback models produce galaxies that move along the MDAR rather than perpendicular to it*, resulting in small scatter. It is easy to see why. Consider an arbitrary galactic radius at which the total and baryonic accelerations are related by eq. 1. Changing the enclosed baryon mass within this radius by a factor f shifts points horizontally by the same factor (to $g^{'}_{\rm bar} = f\,g_{\rm bar}$), but also vertically by $g^{'}_{\rm tot} = g_{\rm tot} + (f-1)\,g_{\rm bar}$. As a result, galaxies of different stellar mass, or whose mass profiles differ, tend to move diagonally in the space of $g_{\rm bar}$ versus $g_{\rm tot}$. The shaded regions in the lower panels of Figure 2 indicate the expected scatter in the MDAR for enclosed baryon masses that differ from eq. 1 (with $g_\dagger = 3 \times 10^{-10}\,m\,s^{-2}$) by factors of ± 3 (light shaded region) and ± 2 (darker region).

Figure 3 (left panel) shows the run of total versus baryonic acceleration for *all* ($z = 0$) galaxies in *all* simulations. We have included here 29 isolated galaxies identified in the APOSTLE Simulation. For clarity, individual radial bins are shown as semi-transparent colored points to indicate the scatter. For each run we also show the median trends either as solid lines (for REF, OnlyAGN and NoAGN) or as heavy symbols (for WeakFB, StrongFB and APOSTLE). The dashed line (eq. 1, with $g_\dagger = 3 \times 10^{-10}\,\rm m\,s^{-2}$) describes the numerical data remarkably well, even for models whose subgrid physics were *not* tuned to match observational constraints, and whose galaxies do not match the observed TF or abundance matching relations. The inset panel, for example, plots the residual scatter around this line, after stacking all halos in each simulation. Despite the wide range of galaxy properties that emerge from

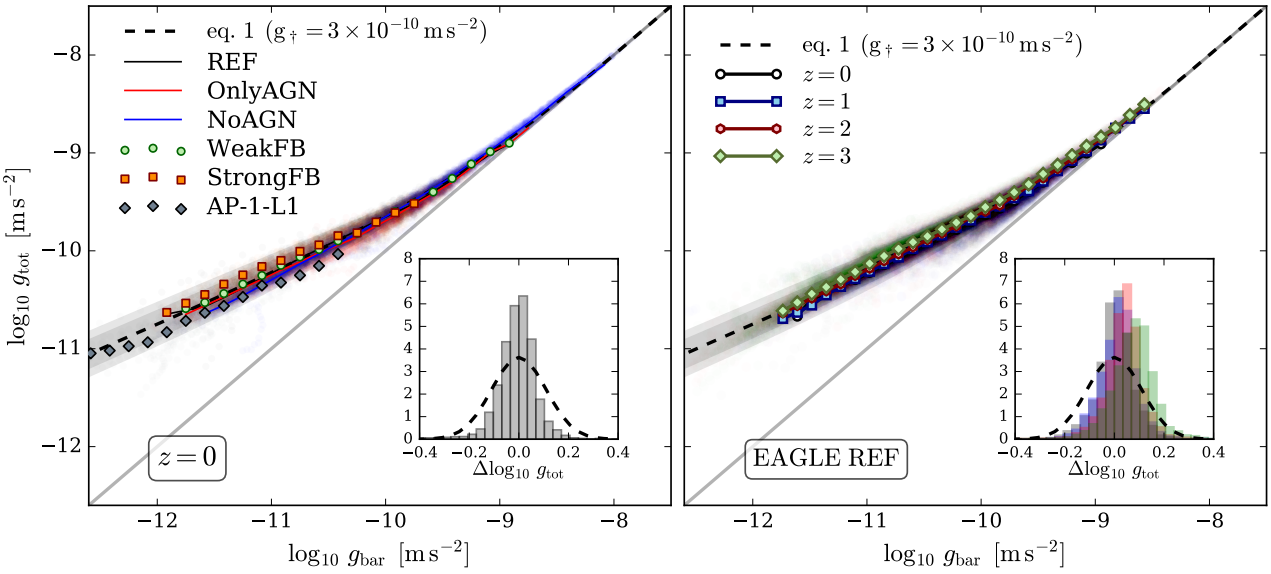

FIG. 3. Total centripetal acceleration profiles for all halos as a function of their baryonic acceleration. The left panel summarizes the results obtained for all of our simulations at $z = 0$. Lines, points and colors have the same meaning as in Figure 1. Also, included are 25 isolated galaxies in the APOSTLE simulation (grey diamonds), that extend the stellar mass range to $\approx 1.5 \times 10^7\,\mathrm{M}_\odot$. The right-hand panel shows (for REF) the redshift evolution for progenitor galaxies at various redshifts. The dashed lines show eq. 1 with $g_\dagger = 3 \times 10^{-10}\,\mathrm{m\,s^{-2}}$; shaded regions highlight the scatter about this line for factors of ±3 (light) and ±2 (dark) changes in enclosed baryon mass. Inset panels show the relative scatter around this curve after combining all simulations (left) and for individual redshifts (right); the heavy dashed lines represent the observational scatter in [10].

our runs, the scatter is smaller ($\sigma = 0.09$ dex; see also [14]) than that of the best available observational data ($\sigma = 0.11$ dex), indicated by the heavy dashed line [10]. We note, however, that the scatter in our runs increases toward lower mass galaxies. If verified observationally, this would be strong evidence in favor of dark matter.

Note too that the acceleration relation persists at high redshift, where galaxies are more likely to be actively merging. The right-hand panel of Figure 3 shows the acceleration relation for galaxy progenitors in our REF model at four different redshifts (defined as the central galaxy of each $z = 0$ halo's main progenitor). Regardless of z, all galaxies follow a similar curve in the space of total versus baryonic acceleration. The residuals are again small (inset panel), but show evidence of a slight but systematic redshift dependence (the mean residual increases slightly with redshift, but remains within the observational error).

DISCUSSION AND SUMMARY

We analyzed a suite of simulations from the EAGLE Project that adopt widely varying subgrid parameters. Some simulations yield populations of galaxies that differ systematically from observed galaxy scaling relations. Nevertheless, all galaxies follow a simple relationship between their total and baryonic acceleration profiles, regardless of the feedback implementation. Different feedback prescriptions, which result in different galaxy populations, force galaxies to move *along* the MDAR rather than perpendicular to it, yielding small scatter.

We note, however, that the total to baryonic acceleration relation depends *slightly but systematically* on the subgrid model. For example, the StrongFB and NoAGN models are, at low acceleration, noticably different: the former lies slightly above the best-fitting eq. 1, the latter slightly below. The differences however are small and within the observational (error-dominated) scatter. The radial acceleration relation given by eq. 1 is, therefore, very forgiving: only *large* departures from any sensible galaxy-halo scaling relations lead to noticeable systematics. The "small" observed scatter in the MDAR is, in fact, quite large, and is unlikely to provide useful constraints on galaxy formation models.

ACKNOWLEDGMENTS

We are indebted to Lydia Heck and Peter Draper, whose technical support and expertise made this project possible. ADL is supported by a COFUND Junior Research Fellowship; RAC is a Royal Society University Research Fellow. JS acknowledges support from the Netherlands Organisation for Scientific Research (NWO), through VICI grant 639.043.409, and the European Research Council under the European Union's Seventh Framework Programme (FP7/2007- 2013) / ERC Grant agreement 278594-GasAroundGalaxies. This

work was supported by the Science and Technology Facilities Council (grant number ST/F001166/1); European Research Council (grant numbers GA 267291 "Cosmiway"). Computing resources were supplied bt the DiRAC Data Centric system at Durham University, operated by the Institute for Computational Cosmology on behalf of the STFC DiRAC HPC Facility (`www.dirac.ac.uk`). This equipment was funded by BIS National E-infrastructure capital grant ST/K00042X/1, STFC capital grant ST/H008519/1, and STFC DiRAC Operations grant ST/K003267/1 and Durham University. DiRAC is part of the National E-Infrastructure. We also acknowledge PRACE for granting us access to the Curie machine based in France at TGCC, CEA, Bruyères-le-Châtel.

* Electronic address: aaron.ludlow@durham.ac.uk
† Senior CIfAR fellow

[1] J. Wang, J. F. Navarro, C. S. Frenk, S. D. M. White, V. Springel, A. Jenkins, A. Helmi, A. Ludlow, and M. Vogelsberger, MNRAS **413**, 1373 (2011), arXiv:1008.5114 [astro-ph.CO].
[2] S. D. M. White and M. J. Rees, MNRAS **183**, 341 (1978).
[3] S. D. M. White and C. S. Frenk, Astrophys. J. **379**, 52 (1991).
[4] R. B. Tully and J. R. Fisher, A&A **54**, 661 (1977).
[5] S. M. Faber and R. E. Jackson, Astrophys. J. **204**, 668 (1976).
[6] C. G. Lacey, C. M. Baugh, C. S. Frenk, A. J. Benson, R. G. Bower, S. Cole, V. Gonzalez-Perez, J. C. Helly, C. D. P. Lagos, and P. D. Mitchell, MNRAS **462**, 3854 (2016), arXiv:1509.08473.
[7] I. Ferrero, J. F. Navarro, M. G. Abadi, L. V. Sales, R. G. Bower, R. A. Crain, C. S. Frenk, M. Schaller, J. Schaye, and T. Theuns, ArXiv e-prints (2016), arXiv:1607.03100.
[8] S. S. McGaugh, Astrophys. J. **609**, 652 (2004), astro-ph/0403610.
[9] J. Janz, M. Cappellari, A. J. Romanowsky, L. Ciotti, A. Alabi, and D. A. Forbes, MNRAS **461**, 2367 (2016), arXiv:1606.05003.
[10] S. McGaugh, F. Lelli, and J. Schombert, ArXiv e-prints (2016), arXiv:1609.05917.
[11] M. Milgrom, ArXiv e-prints (2016), arXiv:1609.06642.
[12] F. C. van den Bosch and J. J. Dalcanton, Astrophys. J. **534**, 146 (2000), astro-ph/9912004.
[13] A. Di Cintio and F. Lelli, MNRAS **456**, L127 (2016), arXiv:1511.06616.
[14] B. W. Keller and J. W. Wadsley, ArXiv e-prints (2016), arXiv:1610.06183.
[15] H. Desmond, ArXiv e-prints (2016), arXiv:1607.01800.
[16] J. Schaye, R. A. Crain, R. G. Bower, M. Furlong, M. Schaller, T. Theuns, C. Dalla Vecchia, C. S. Frenk, I. G. McCarthy, J. C. Helly, A. Jenkins, Y. M. Rosas-Guevara, S. D. M. White, M. Baes, C. M. Booth, P. Camps, J. F. Navarro, Y. Qu, A. Rahmati, T. Sawala, P. A. Thomas, and J. Trayford, MNRAS **446**, 521 (2015), arXiv:1407.7040.
[17] R. A. Crain, J. Schaye, R. G. Bower, M. Furlong, M. Schaller, T. Theuns, C. Dalla Vecchia, C. S. Frenk, I. G. McCarthy, J. C. Helly, A. Jenkins, Y. M. Rosas-Guevara, S. D. M. White, and J. W. Trayford, MNRAS **450**, 1937 (2015), arXiv:1501.01311.
[18] Planck Collaboration, P. A. R. Ade, N. Aghanim, C. Armitage-Caplan, M. Arnaud, M. Ashdown, F. Atrio-Barandela, J. Aumont, C. Baccigalupi, A. J. Banday, and et al., A&A **571**, A16 (2014), arXiv:1303.5076.
[19] V. Springel, MNRAS **364**, 1105 (2005), astro-ph/0505010.
[20] V. Springel, S. D. M. White, G. Tormen, and G. Kauffmann, MNRAS **328**, 726 (2001), astro-ph/0012055.
[21] K. Dolag, S. Borgani, G. Murante, and V. Springel, MNRAS **399**, 497 (2009), arXiv:0808.3401.
[22] A. Fattahi, J. F. Navarro, T. Sawala, C. S. Frenk, K. A. Oman, R. A. Crain, M. Furlong, M. Schaller, J. Schaye, T. Theuns, and A. Jenkins, MNRAS **457**, 844 (2016), arXiv:1507.03643.
[23] T. Sawala, C. S. Frenk, A. Fattahi, J. F. Navarro, R. G. Bower, R. A. Crain, C. Dalla Vecchia, M. Furlong, J. C. Helly, A. Jenkins, K. A. Oman, M. Schaller, J. Schaye, T. Theuns, J. Trayford, and S. D. M. White, MNRAS **457**, 1931 (2016), arXiv:1511.01098.